

Broadband-tunable LP₀₁ mode frequency shifting by Raman coherence waves in H₂-filled hollow-core PCF

S. T. BAUERSCHMIDT,* D. NOVOA, A. ABDOLVAND, AND P. ST.J. RUSSELL

Max Planck Institute for the Science of Light, Guenther-Scharowsky Strasse 1, 91058 Erlangen, Germany

*Corresponding author: sebastian.bauerschmidt@mpl.mpg.de

When a laser pump beam of sufficient intensity is incident on a Raman-active medium such as hydrogen gas, a strong Stokes signal, red-shifted by the Raman transition frequency Ω_R , is generated. This is accompanied by the creation of a "coherence wave" of synchronized molecular oscillations with wavevector $\Delta\beta$ determined by the optical dispersion. Within its lifetime, this coherence wave can be used to shift by Ω_R the frequency of a third "mixing" signal, provided phase-matching is satisfied, i.e., $\Delta\beta$ is matched. Conventionally this can be arranged using non-collinear beams or higher-order waveguide modes. Here we report collinear phase-matched frequency shifting of an arbitrary mixing signal using only the fundamental LP₀₁ modes of a hydrogen-filled hollow-core PCF. This is made possible by the S-shaped dispersion curve that occurs around the pressure-tunable zero dispersion point. Phase-matched frequency shifting by 125 THz is possible from the UV to the near-IR. Long interaction lengths and tight modal confinement reduce the peak intensities required, allowing conversion efficiencies in excess of 70%. The system is of great interest in coherent anti-Stokes Raman spectroscopy and for wavelength-conversion of broadband laser sources.

Coherence waves (C_w 's) of collective molecular oscillation, created by stimulated Raman scattering (SRS) [1-5], are useful in the synthesis of ultrashort pulses [6] and for efficient frequency conversion [3-5]. They arise through the beating between two intense quasi-monochromatic laser beams whose frequencies differ by the Raman transition frequency Ω_R . The resulting C_w takes the form of a travelling refractive index grating. Under phase-matched conditions, an arbitrarily weak mixing signal at a different wavelength can be scattered off this C_w , which is coherently amplified when the mixing signal is down-shifted by Ω_R , and absorbed when the mixing signal is up-shifted by Ω_R [2-5].

Phase-matching can be achieved using non-collinear beams in bulk materials [7, 8] or higher-order guided modes in optical fibers [5, 9]. Broadband-guiding kagomé-style hollow-core photonic crystal fiber (kagomé-PCF) is particularly attractive since the dispersion can be precisely controlled by varying the gas pressure

[10]. In addition, tight modal confinement and long light-gas interaction lengths dramatically reduce the peak laser intensities required for efficient excitation of C_w 's.

In this Letter we report how a C_w , excited by an LP₀₁ pump pulse in hydrogen-filled kagomé-PCF, can be used, within its coherence lifetime, for efficient phase-matched frequency-shifting of an LP₀₁ mixing pulse at an entirely different wavelength. The process is made possible by the unique S-shaped dispersion curve that forms around the pressure-tunable zero dispersion point (ZDP) in kagomé-PCF [10].

To illustrate the concept, the dispersion curve in the vicinity of a ZDP at wavevector β_0 and frequency ω_0 is drawn schematically in Fig. 1, assuming no dispersion terms higher than third-order. A C_w is first "written" by pump and Stokes waves, labeled by W_0 and W_{-1} on the diagram. The ω - β "four vector" of the resulting C_w is marked by the blue dashed line. Once created, this C_w can be used for fully phase-matched frequency up-conversion to point M_1 of an optical mixing signal at point M_0 on the opposite side of the ZDP. It may also be used to seed frequency down-conversion to M_0 of a signal at M_1 , during which process it will be amplified. This procedure will of course also work the other way around, i.e., with writing signals on the low-frequency side of the ZDP and mixing signals on the high-frequency side.

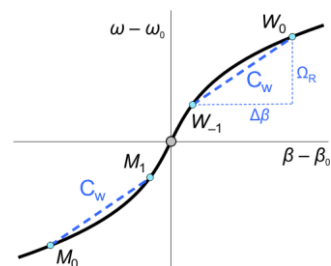


Fig. 1. (a) Sketch of the dispersion of a gas-filled kagomé-PCF in the vicinity of the ZDP (the grey dot at $\omega = \omega_0$ and $\beta = \beta_0$), assuming no dispersion terms higher than third-order. The blue dashed lines indicate the coherence wave C_w excited by the writing signals W_0 and W_{-1} . C_w is a four-vector with frequency Ω_R and wavevector $\Delta\beta$ given by the difference between the wavevectors of the writing signals. It can be used either to up-shift the frequency of a mixing signal M_0 placed at the position symmetric to W_0 on the opposite side of the ZDP or to seed down-conversion of a signal placed at M_1 .

In general, higher-order dispersion will increasingly distort the perfect S-shape as one moves further away from the ZDP. Nevertheless, as we shall see, it is always possible to find two distinct pairs of points, albeit asymmetrically placed about the ZDP, that are connected by the identical C_w . If the frequency of the mixing

beam is not precisely correct, however, the up-conversion process will be dephased at a rate given by:

$$\mathcal{D} = \Delta\beta - (\beta_{M_1} - \beta_{M_0}) \quad (1)$$

where the full dispersion relation of the LP₀₁ mode must be taken into account. Its propagation constant β_{01} can be approximated to good accuracy by:

$$\beta_{01} = \sqrt{k_0^2 n_{\text{gas}}^2(p, \lambda) - u^2 / a^2(\lambda)} \quad (2)$$

where $k_0 = 2\pi/\lambda$ is the vacuum wavevector, n_{gas} is the refractive index of the filling gas, p is the gas pressure, $u = 2.405$ for the fundamental core mode and $a(\lambda) = a_{\text{AP}}(1 + s\lambda^2/(a_{\text{AP}}d))$, where a_{AP} is the area-preserving core radius, $s = 0.08$ is an empirical dimensionless parameter and d is the core-wall thickness [11]. This dispersion relation is plotted in Fig. 2(a) at three different pressures for the fiber used in the experiments ($a_{\text{AP}} = 23.4 \mu\text{m}$ and $d = 97 \text{ nm}$). In order to magnify the very flat S-shape, we have subtracted off the linear dispersion by plotting frequency versus $(\beta_{\text{ref}} - \beta)$, where β_{ref} is a pressure-dependent linear function of frequency chosen such that $(\beta_{\text{ref}} - \beta)$ is zero at 800 THz.

The wavelength of the ZDP shifts from $\sim 400 \text{ nm}$ to $\sim 1.1 \mu\text{m}$ as the pressure increases from 1 to 100 bar [Fig. 2(b)].

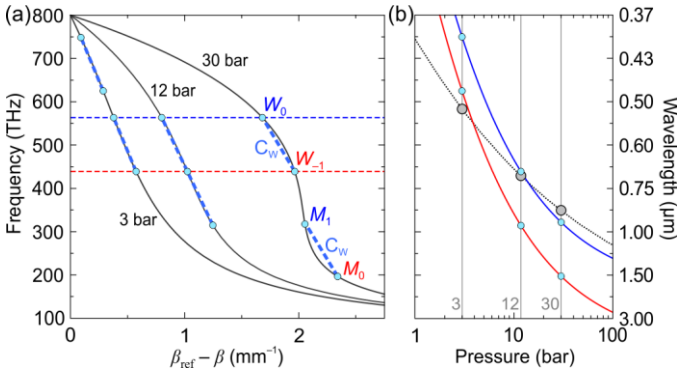


Fig. 2. (a) Dispersion curves of the LP₀₁ mode for pressures of 3, 12, and 30 bar (see text). The notation is the same as in Fig. 1, and for clarity only the 30 bar case is fully labeled. (b) Phase-matched frequency pairs (solid lines) and ZDPs (dotted line) as a function of pressure for a pump frequency (W_0) of 563 THz (532 nm). The ZDPs for the three pressures in (a) are marked with grey dots.

The mixing frequencies of perfectly phase-matched pairs can be accurately calculated by solving Eqs. 1 and 2. Figure 2(a) shows the C_w 's created at three different pressures by beating a pump signal W_0 at 532 nm (563 THz) with a Stokes signal W_{-1} at 685 nm (438 THz). The presence of higher-order dispersion shifts the positions of the two perfectly phase-matched pairs asymmetrically about the ZDP. At 30 bar both pump (W_0) and Stokes (W_{-1}) signals lie in the normal dispersion region ($\omega > \omega_0$), and the phase-matched mixing pair (M_1, M_0) is at (322, 197) THz in the anomalous dispersion region. At 3 bar, on the other hand, the C_w is excited in the anomalous dispersion region and the mixing pair is phase-matched at (749, 624) THz in the normal dispersion region.

A special situation occurs at 12 bar, when the lower frequency of the upper pair and the upper frequency of the lower pair coincide; this causes a strong second Stokes (W_{-2}) signal to appear when pumping with W_0 (see below). Overall, Fig. 2 shows that, for a fixed W_0 frequency of 563 THz, the frequency of M_1 for perfect phase-matching can be tuned from the UV to the near IR simply by changing the pressure.

To confirm these predictions experimentally, we developed a set-up for exciting and probing C_w 's under different conditions [see Fig.

3]. The output of a linearly-polarized 1064 nm laser, delivering ns pulses, was split into two parts. The first part was used to generate the W_0 signal by frequency-doubling to 532 nm in a KTP crystal. The second was spectrally broadened to $\sim 350 \text{ nm}$ in a 4-m-long solid-core PCF, and used as the M_0 mixing signal. The pulse durations were 3.2 ns for W_0 and 2.0 ns for M_0 . Both pulses were then recombined and launched into the LP₀₁ mode of a 1 m long gas-filled kagomé-PCF. The signals exiting the fiber endface were monitored using an optical spectrum analyzer and imaged using a CCD camera. The intensity of the mixing beam was kept low so as to avoid the onset of SRS, which would influence the C_w . The interaction was found to be strongest when the mixing pulse was delayed by $\sim 1 \text{ ns}$ from the pump pulse.

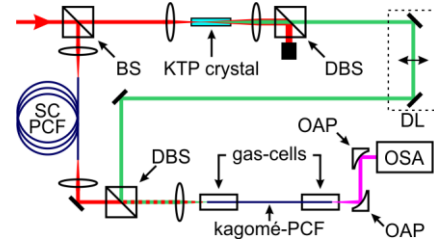


Fig. 3. Schematic of the experimental setup. BS: beam-splitter; DBS: dichroic beam-splitter; OAP: off-axis parabolic mirror; SC-PCF: solid-core photonic crystal fiber; DL: delay line; OSA: optical spectrum analyzer.

The vibrational Raman gain of hydrogen saturates for pressures above $\sim 10 \text{ bar}$ [12]. In this regime the behavior of the system is dominated by changes in the phase-matching conditions. Below 10 bar both the phase-matching conditions and the Raman gain are pressure dependent and play a role.

We recorded the spectra generated when scanning the pressure from 5 to 40 bar, for two pulse energies: $E_p = 20$ and $30 \mu\text{J}$ [Fig. 4]. The photon rates in the W_0 , W_{-1} and W_{-2} bands are plotted in Figs. 4(a&c) and those in the mixing signals in Figs. 4(b&d). Note that, for clarity, the sum of the rates in the two up-shifted sidebands M_1 at 730 nm (411 THz) and M_2 at 560 nm (535 THz) is plotted, along with the signal M_0 at 1048 nm (286 THz); the full experimental data is available in Fig. S2 of Supplement 1.

In Fig. 4(a) the pump pulse energy was $E_p = 20 \mu\text{J}$ (injected into the kagomé-PCF with $\sim 40\%$ coupling efficiency). As the pressure increases, W_0 converts to W_{-1} via SRS, giving rise to a C_w and becoming significantly depleted. At 12 bar W_{-1} is itself depleted and light appears at the W_{-2} frequency (i.e., the second Stokes). This is because at this pressure both the $W_0 \rightarrow W_{-1}$ and $W_{-1} \rightarrow W_{-2}$ processes are phase-matched to the same C_w . At higher pressures the $W_{-1} \rightarrow W_{-2}$ phase-mismatch increases and the W_{-2} signal drops again.

At 14.2 bar, the C_w created in the $W_0 \rightarrow W_{-1}$ process is able to phase-match $M_0 \rightarrow M_1$ conversion from 1048 to 730 nm, with photon number conversion efficiencies (based on depletion of the M_0 signal) well above 50% at the peak [Fig. 4(b)].

At 30 μJ pump pulse energy, a strong W_{-2} signal appears for pressures above 15 bar [Fig. 4(c)]. This is because the W_{-1} signal is strong enough to reach the threshold for SRS, generating a strong W_{-2} signal and an independent C_w . This new C_w causes a new phase-matching point to appear at a pressure of $\sim 27 \text{ bar}$, resulting in a second peak of $M_0 \rightarrow M_1$ conversion [Fig. 4(d)]. At the same time the first conversion peak reaches a conversion efficiency above 70%.

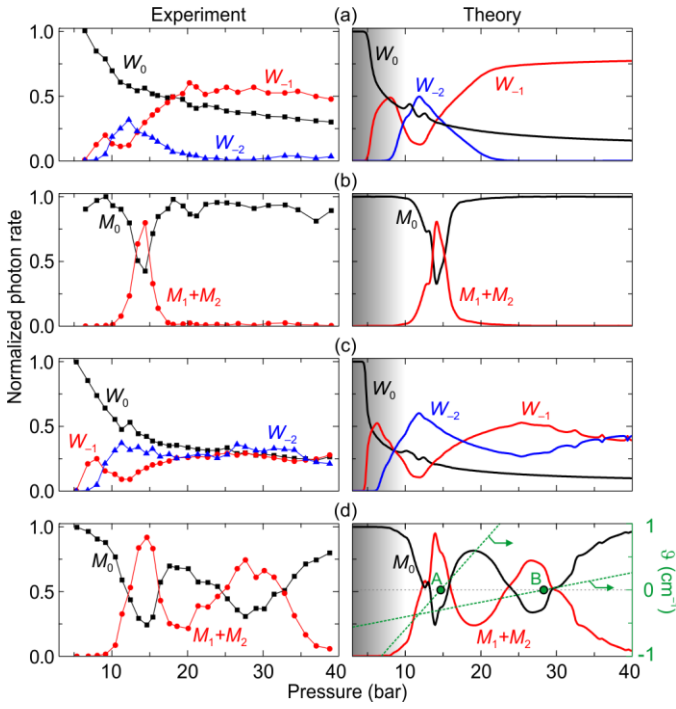


Fig. 4. Experimental and theoretical normalized photon rates of the various signals, plotted against increasing pressure. (a) Pump (W_0), first (W_{-1}) and second (W_{-2}) Stokes waves for $E_p = 20 \mu\text{J}$. (b) Mixing (M_0) and up-shifted anti-Stokes ($M_1 + M_2$) signals, coupled by the C_w 's created in (a). (c) Pump (W_0), first (W_{-1}) and second (W_{-2}) Stokes waves for $E_p = 30 \mu\text{J}$. (d) Mixing (M_0) and up-shifted anti-Stokes ($M_1 + M_2$) signals, coupled by the C_w 's created in (c). The green lines show the pressure-dependence of the phase-match parameter ϑ . Note that the C_w generated by $W_{-1} \rightarrow W_{-2}$ conversion creates a second phase-matching pressure at point B. Up-shifting to M_1 is most efficient at the phase-matching pressures (points A and B).

As seen in the right-hand column of Fig. 4, these measurements are in good overall agreement with numerical solutions of a set of coupled spatio-temporal Maxwell-Bloch equations [13]. Note that the model is only valid for pressures above 10 bar, i.e., outside the shaded region in Fig. 4, when the Raman gain is independent of pressure [see Supplement 1 for details].

The simulations also allow us to study the behavior of the C_w amplitude $|Q|$, a quantity that is not accessible in the experiment. Figure 5 plots the evolution of both $|Q|$ and the $(M_1 + M_2)$ photon rate along the fiber at gas pressures of 12 and 27 bar for $E_p = 30 \mu\text{J}$. At 12 bar $|Q|$ grows through SRS-related exponential gain in the W_{-1} signal [upper left-hand panel in Fig. 5]. It peaks at ~ 40 cm, decreasing thereafter because by that point the majority of pump photons have been converted to the W_{-1} band. Note that the temporal peak of $|Q|$ is delayed by ~ 1 ns relative to the center of the pump pulse, as expected in transient Raman scattering. For this special pressure (as explained above in Fig. 2) the same C_w is simultaneously able to seed down-conversion from the W_{-1} to the W_{-2} band (and thus be amplified), giving rise to the strong W_{-2} signals observed in Figs. 4(a&c). As expected, up-conversion from the M_0 to the M_1 band is highest when $|Q|$ is strongest [upper right-hand panel in Fig. 5].

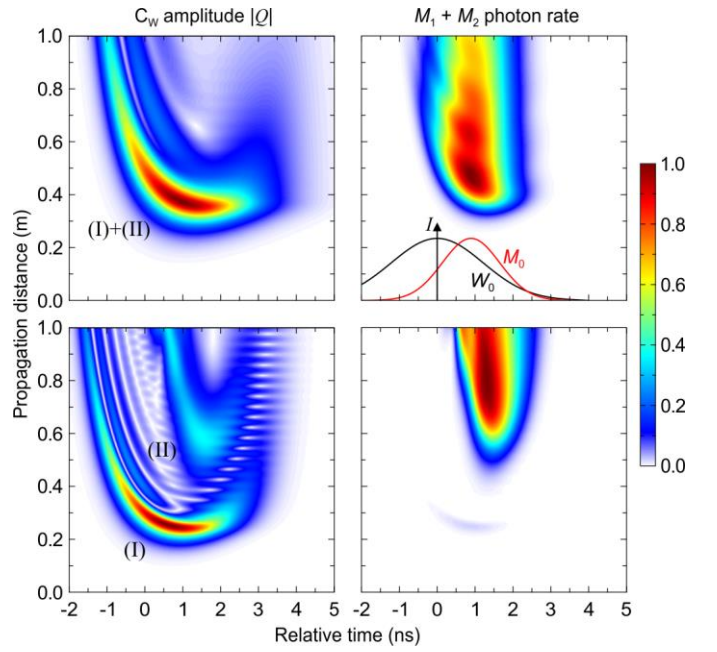


Fig. 5. Simulated spatio-temporal evolution of the normalized C_w amplitude $|Q|$ and normalized $(M_1 + M_2)$ photon rate for $E_p = 30 \mu\text{J}$ at pressures of 12 bar (upper) and 27 bar (lower). C_w 's created in the $W_0 \rightarrow W_{-1}$ process are marked with (I) and those created by the $W_{-1} \rightarrow W_{-2}$ process with (II). The inset in the upper right panel shows the normalized temporal profiles of the W_0 and M_0 pulses at entrance to the fiber. Time is relative to a frame traveling at the group velocity of the W_0 pulse. The origin of the periodic oscillations in the lower left panel is discussed in Supplement 1.

This special dual phase-matching condition is no longer valid at 27 bar, because the $W_0 \rightarrow W_{-1}$ and $W_{-1} \rightarrow W_{-2}$ conversion processes produce different C_w 's. As a result, the first peak in $|Q|$ at ~ 25 cm originates from $W_0 \rightarrow W_{-1}$, whereas the second peak at ~ 60 cm is created by $W_{-1} \rightarrow W_{-2}$ conversion and appears at a later time [lower left-hand panel in Fig. 5]. For the mixing beams, although $M_0 \rightarrow M_1$ conversion is very weak at the 25 cm point due to strong dephasing ($\vartheta = 1.6 \text{ cm}^{-1}$), it is strong at 60 cm because of phase-matching with the second C_w (lower right-hand panel in Fig. 5). This illustrates the supreme importance of phase-matching for efficient frequency conversion.

From coupled mode theory, the bandwidth $\Delta\nu$ of the up-conversion process covers the range $-\pi < \vartheta L_c < \pi$ where L_c is the length over which the C_w amplitude is significant (~ 10 cm in the experiments). $\Delta\nu$ depends on the curvature of the dispersion curve for the $M_0 \rightarrow M_1$ process and ranges from ~ 250 THz for M_0 at 800 THz, to ~ 20 THz for M_0 at 300 THz. These large bandwidths make it possible to frequency-shift and replicate broadband signals, as seen in Fig. 6 where the full recorded spectrum at 14.5 and 27.6 bar is plotted for $E_p = 30 \mu\text{J}$. Cascaded up-shifting to the M_2 band is possible in the case of 14.5 bar [upper panel in Fig. 6] because of the relatively flat dispersion curve from ~ 300 to ~ 600 THz [see for instance the 12 bar curve in Fig. 2(a)]. In contrast, at 27.6 bar efficient conversion is only possible to the first (M_1) sideband (lower panel in Fig. 6), owing to the strong curvature of the dispersion over the whole frequency range [see for instance the 30 bar curve in Fig. 2(a)].

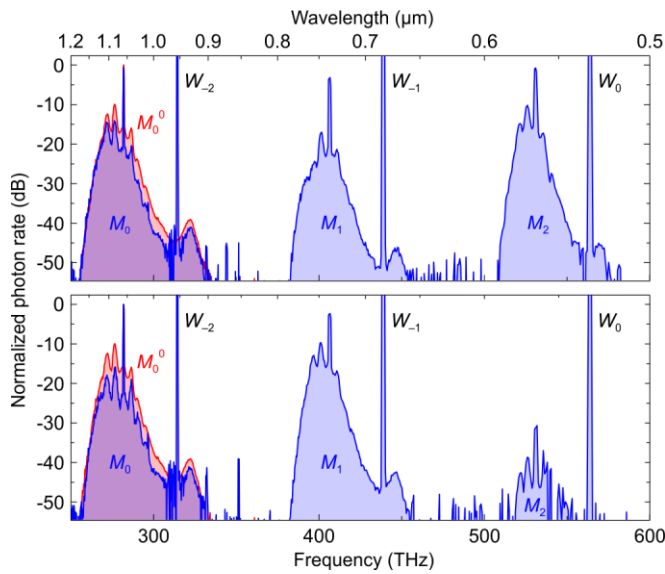


Fig. 6. Demonstration of broadband frequency shifting for 14.5 bar (upper panel) and 27.6 bar (lower panel). The broadband mixing signal M_0 is frequency up-shifted to the first (M_1) and second (M_2) anti-Stokes bands. The original spectrum M_0^0 (pump switched off) is depleted accordingly. The photon rates are normalized to the peak of the broadband mixing M_0^0 signal at 1064 nm.

Since ϑ is also a function of pressure, it determines the width of the conversion peaks as seen in Fig. 4(d), where ϑ is plotted for the two C_w 's excited in that case. It is clear that a weaker pressure dependence of ϑ translates into broader conversion peaks.

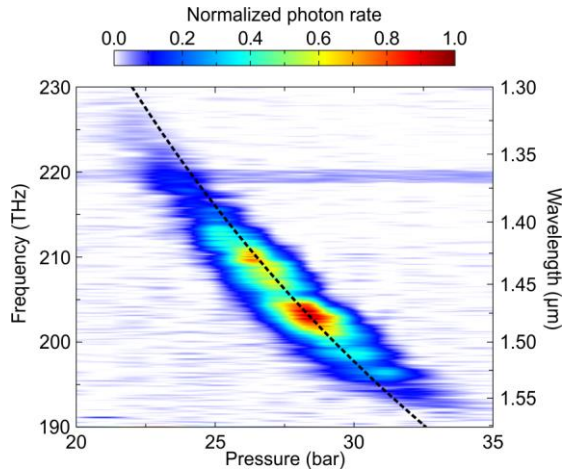


Fig. 7. Frequency down-shifted signal versus pressure. The dashed line represents the theoretical perfectly phase-matched frequencies.

In this Letter we have concentrated on frequency up-shifting. As mentioned in the introduction, it is also possible to use a C_w to frequency down-shift a mixing signal. In this case the C_w acts as a (potentially very strong) seed, being amplified in the conversion process. In Fig. 7 we show the result of an experiment with the same setup where a broadband signal at ~ 325 THz (920 nm) is down-shifted. The maximum conversion efficiency achieved is $\sim 25\%$. Note also that, since the phase-matching frequency shifts with pressure, so does the peak of the down-shifted frequency band. The experimental trace nicely follows the analytical curve for perfect phase-matching [the dashed curve in Fig. 7]. Taken together with all-LP₀₁ operation, this further demonstrates the wide usable frequency range and versatility of this unique wavelength converter.

In conclusion, the S-shaped dispersion curve in the vicinity of the ZDP makes hydrogen-filled kagomé-PCF an ideal vehicle for highly efficient wavelength conversion of broad-band optical signals. A coherence wave (which behaves like a travelling refractive index grating) is first excited by SRS on one side of the ZDP. It is then used for phase-matched conversion of a signal on the opposite side of the ZDP. The system is widely pressure tunable, permitting highly efficient up and down-conversion, by 125 THz, of LP₀₁ signals from the UV to the near-IR. The system offers a new route for frequency conversion of ultrashort laser pulses from mode-locked lasers. Further flexibility is possible by changing the fiber design, working with different Raman active gases, adding buffer gases or working with a different pump wavelength. This uniquely flexible system has many potential applications in ultrasensitive Raman spectroscopy and laser science.

See Supplement 1 for supporting content.

REFERENCES

1. S. E. Harris and A. V. Sokolov, *Phys. Rev. Lett.* **81**, 2894 (1998).
2. A. Nazarkin, G. Korn, M. Wittmann, and T. Elsaesser, *Phys. Rev. Lett.* **83**, 2560 (1999).
3. J. Q. Liang, M. Katsuragawa, F. L. Kien, and K. Hakuta, *Phys. Rev. Lett.* **85**, 2474 (2000).
4. J. J. Weber, J. T. Green, and D. D. Yavuz, *Phys. Rev. A* **85**, 013805 (2012).
5. S. T. Bauerschmidt, D. Novoa, B. M. Trabold, A. Abdolvand, and P. St.J. Russell, *Opt. Express* **22**, 20566 (2014).
6. S. Baker, I. A. Walmsley, J. W. G. Tisch, and J. P. Marangos, *Nature Photon.* **5**, 664 (2011).
7. A. C. Eckbreth, *Appl. Phys. Lett.* **32**, 421 (1978).
8. T. Wilhelm, J. Piel, and E. Riedle, *Opt. Lett.* **22**, 1494 (1997).
9. J. Demas, P. Steinvurzel, B. Tai, L. Rishøj, Y. Chen, and S. Ramachandran, *Optica* **2**, 14 (2015).
10. P. St.J. Russell, P. Holzer, W. Chang, A. Abdolvand, and J. C. Travers, *Nature Photon.* **8**, 278 (2014).
11. M. Finger, N. Y. Joly, T. Weiss, and P. St.J. Russell, *Opt. Lett.* **39**, 821 (2014).
12. W. K. Bischel and M. J. Dyer, *J. Opt. Soc. Am. B* **3**, 677 (1986).
13. M. G. Raymer and I. A. Walmsley, in *Prog. Optics*, (Elsevier, 1990), p. 181.

Broadband-tunable LP₀₁ mode frequency shifting by Raman coherence waves in H₂-filled hollow-core PCF: supplementary material 1

S. T. BAUERSCHMIDT,* D. NOVOA, A. ABDOLVAND, AND P. ST.J. RUSSELL

Max Planck Institute for the Science of Light, Guenther-Scharowsky Strasse 1, 91058 Erlangen, Germany

*Corresponding author: sebastian.bauerschmidt@mpl.mpg.de

We describe the theoretical model employed to simulate the dynamics of the system and show the individual photon rates of the first two up-shifted sidebands (M_1 and M_2), where only their sum was shown in the main text. In addition, we also provide details on the pressure dependence of the interference of two coherence waves.

1. Numerical simulations

To simulate the spatio-temporal dynamics of the C_w amplitude Q and the optical fields, we used a semi-classical treatment of stimulated Raman scattering [1] based on the following set of coupled Maxwell-Bloch equations:

$$\begin{aligned} \frac{\partial}{\partial z} E_l = & -i\kappa_{2,l-1} Q E_{l-1} q_{l-1} q_l^* \frac{\omega_l}{\omega_{l-1}} \\ & -i\kappa_{2,l} Q^* E_{l+1} q_{l+1} q_l^* - \frac{1}{2} \alpha_l E_l \end{aligned} \quad (\text{S1})$$

$$\frac{\partial}{\partial t} Q = -Q/T_2 + in \frac{1}{4} \sum_l \kappa_{1,l} E_l^* E_{l+1} q_l^* q_{l+1}, \quad (\text{S2})$$

where the integer index l denotes the Raman sideband of the pump at frequency $\omega_l = \omega_W + l\Omega_R$ (ω_W is the frequency of the pump). The complex electric field amplitudes $e_l(z, \tau)$ are described in terms of the slowly varying envelopes $E_l(z, \tau)$:

$$e_l(z, \tau) = E_l(z, \tau) q_l = E_l(z, \tau) e^{i\beta_l z} \quad (\text{S3})$$

where the propagation constants β_l are calculated using Eq. 2 in the main text. The parameters α_l are the attenuation constants of the different spectral lines. We assume the population difference is $n = -1$, i.e., the majority of the molecules remain in the ground state, which is a reasonable approximation since the highest value of coherence $|Q|$ reached in the experiments is ~ 0.01 . The frequency-dependent coupling coefficients $\kappa_{1,l}$ and $\kappa_{2,l}$ can be derived from the experimentally determined gain values γ [2] by:

$$\kappa_{1,l} = \sqrt{\frac{2\gamma c^2 \epsilon_0^2}{NT_2 \hbar \omega_l}} \quad (\text{S4})$$

and

$$\kappa_{2,l} = \frac{N \hbar \omega_l \kappa_{1,l}}{2\epsilon_0 c}, \quad (\text{S5})$$

where N is the molecular number density, c is the speed of light in vacuum, ϵ_0 is the vacuum permittivity, \hbar is Planck's constant and T_2 is the dephasing time of the molecules, given in terms of the linewidth $\Delta\nu \sim 1/T_2\pi$ of the Raman transition [2, 3].

To model the dynamics of the mixing beam fields E_m ($\omega_m = \omega_M + m\Omega_R$, where m is an integer) we used the same set of coupled field equations as for the pump (Eq. S1), except that Q takes the value set by SRS in the preparation stage. Since the mixing fields are weak, they are assumed to have no effect on the C_w amplitude (for stronger mixing fields significant amplification or attenuation of Q will occur). Also, since the pulse lengths are comparable to the fiber length (1 m) group velocity walk-off between the different spectral lines is negligible.

The first Stokes signal is generated from noise in the experiment, initiating all the observed dynamics. In the simulations we assume a uniform noise floor of $E_{\text{noise}} = 500$ V/m for all the Raman lines except $l = 0$. We checked the validity of this assumption by measuring the Stokes intensity as a function of pump intensity and extrapolating the exponential growth of the Stokes signal for low pump intensities. This yielded a value close to $E_{\text{noise}} = 500$ V/m for zero pump signal.

The initial shape of the W_1 pulse was assumed to be Gaussian and the modal intensity distribution was modeled by a uniform transverse profile with an effective mode area of $A_{\text{eff}} = 1.5a^2$ [4], where a is the core radius in the kagomé-PCF. Finally, we considered the same pump energies in both simulations and experiments.

The attenuation coefficients at the wavelengths used in the experiments were extracted from the loss measurement shown in Fig. S1.

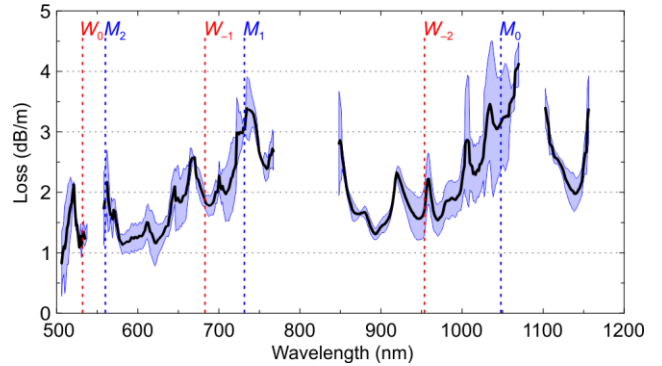


Fig. S1. Measured loss of the HC-PCF (solid line) with estimated error (shaded region). Wavelength ranges without data have loss > 5 dB/m or no loss data are available. The frequency bands used in the Letter are highlighted by the vertical dashed lines.

2. Separate photon rates of up-shifted sidebands

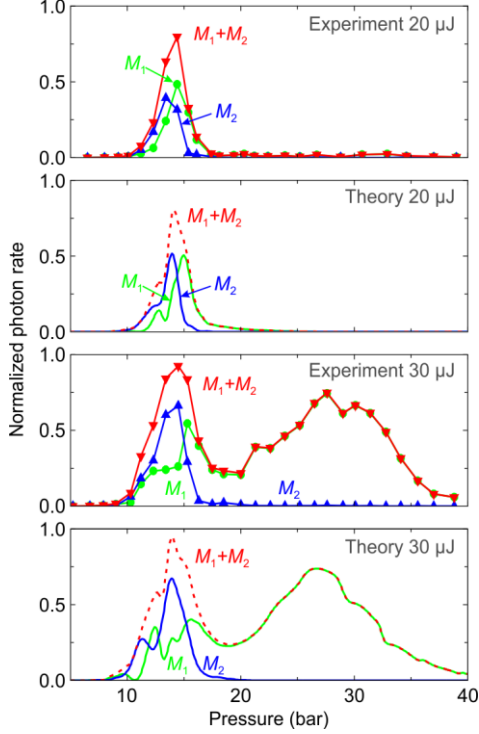


Fig. S2. Experimental and theoretical normalized photon rates of the first (M_1) and second (M_2) mixing sidebands, plotted against increasing pressure (normalized to the maximum of the M_0 rate, not shown) for pump pulse energies E_p of 20 and 30 μJ . Also the sum of both signals ($M_1 + M_2$) is included which was shown in Fig. 3.

In the Letter we restrict the discussion on the dynamics of the mixing beam to the $M_0 \rightarrow M_1$ conversion process, although subsequent scattering to the second sideband ($M_1 \rightarrow M_2$) is also possible (see also Fig. 7 in the main text). Therefore we plot in Fig. 4 of the main text only the sum of the two upshifted signals ($M_1 + M_2$) for clarity. In Fig. S2 we show for completeness the photon rates of the two individual signals together with their sum. Due to the relatively flat dispersion at the phase-matching pressure of the $M_0 \rightarrow M_1$ transition (12 bar, see Fig. 2 in the main text) photons can subsequently be up-shifted from the first to the second sideband giving rise to the M_2 signal in Fig. S2 at ~ 12 bar. In contrast, at 30 bar the dispersion is no longer flat and scattering to the M_2 band is strongly suppressed. No significant M_3 signal was observed in our experiments.

3. Coherence wave interference

The periodic pattern along z observed in the coherence at 27 bar in Fig. 5 is caused by interference of the two coherence waves excited in the system. The observed beat length $L_B = 3.9$ cm agrees well with the value predicted from the dispersion relation for the light, given by:

$$L_B = \frac{2\pi}{\Delta\beta_{(W_0 \rightarrow W_{-1})} - \Delta\beta_{(W_{-1} \rightarrow W_{-2})}}. \quad (\text{S6})$$

Fig. S3 shows how these interference fringes change with pressure and propagation distance for a pump pulse energy of 30 μJ and $\tau = 2$ ns. At the dual phase-matching pressure of 12 bar, $L_R \rightarrow \infty$ and no fringes are visible along z , whereas for increasing pressures spatial oscillations of $|Q|$ are observed. These oscillations decrease in period as the pressure (and therefore the phase-mismatch) increases. In addition, the onset of the $W_{-1} \rightarrow W_{-2}$ coherence wave is also affected by the increasing phase mismatch; as the pressure increases, this C_w moves closer to the fiber endface because coupling from W_{-1} to W_{-2} by the $W_0 \rightarrow W_{-1}$ coherence wave becomes less efficient. Thus, the phase-matched conversion process at 12 bar turns smoothly into a cascaded process where the second Stokes band is generated via SRS from the first Stokes band. Note that the growth of the C_w amplitude is retarded for pressures below 10 bar because of decreasing gain, which prevents clear identification of the interference fringes.

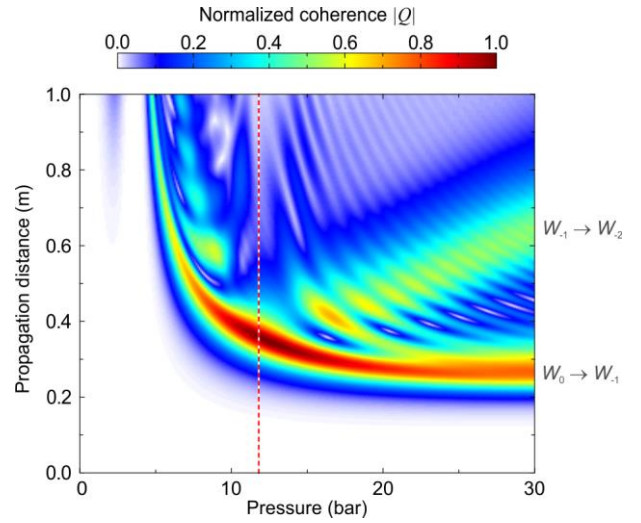


Fig. S3. Amplitude of the coherence $|Q|$ at fixed time $\tau = 2$ ns as a function of pressure and propagation distance. The dashed vertical line marks the pressure where the two C_w 's are identical.

References

1. M. G. Raymer and I. A. Walmsley, "III The Quantum Coherence Properties of Stimulated Raman Scattering," in *Prog. Optics*, E. Wolf, (Elsevier, 1990), p. 181.
2. W. K. Bischel and M. J. Dyer, "Wavelength dependence of the absolute Raman gain coefficient for the Q(1) transition in H₂," *J. Opt. Soc. Am. B* **3**, 677 (1986).
3. J. F. Reintjes, *Handbook of Laser Science and Technology, Supplement 2: Optical Materials* (CRC, 1995).
4. J. C. Travers, W. Chang, J. Nold, N. Y. Joly, and P. St.J. Russell, "Ultrafast nonlinear optics in gas-filled hollow-core photonic crystal fibers," *J. Opt. Soc. Am. B* **28**, A11 (2011).